Nano Energy 40 (2017) 566–575

Contents lists available at ScienceDirect

Nano Energy

journal homepage: www.elsevier.com/locate/nanoen

Full paper

Understanding the phase transitions in spinel-layered-rock salt system: Criterion for the rational design of LLO/spinel nanocomposites

Yi Pei[a,b,1], Qing Chen[a,c,1], Yu-Chen Xiao[a], Li Liu[b], Cheng-Yan Xu[a,*], Liang Zhen[a], Graeme Henkelman[c], Guozhong Cao[b,*]

[a] School of Materials Science and Engineering, Harbin Institute of Technology, Harbin 150001, China
[b] Department of Materials and Engineering, University of Washington, Seattle, WA 98195-2120, United States
[c] Department of Chemistry and the Institute for Computational Engineering and Sciences, The University of Texas at Austin, Austin, TX 78712-0165, United States

ARTICLE INFO

Keywords:
Lithium-ion batteries
Li-rich layered materials
Layered/spinel composite
Density functional theory

ABSTRACT

$xLi_2MnO_3{\cdot}(1-x)LiMO_2$ (LLO)/spinel nanocomposites are of substantial interest as cathodes with high capacity and enhanced conductivity. However, their electrochemical properties are significantly influenced by the complex phase constitutions, and undesired by-products such as rock salt phase could not be efficiently avoided. By ex-/*in-situ* XRD, we revealed the three phase transitions during the decomposition reaction of spinel phase, namely, Li-rich spinel (S_L) to LLO (L), normal spinel (S_N) to rock salt (R) and rock salt to LLO. Density functional theory calculations suggest that Li migrates from the 8a tetrahedral site to the interstitial 16c octahedral site as oxygen is released from S_L and S_N, forming quasi-Li_2MnO_3 and quasi-rock salt crystals, respectively. The dynamic priority of each reaction determined by experiments and calculations was utilized to design the LLO/spinel composites, and a composite with more spinel phase (7.6%) demonstrated high capacity retention at high rates. Our study sheds light on the mechanism of phase transitions among the spinel-layered-rock salt system and reveal the thermodynamic and dynamic priority of each reaction, facilitating the rational design of LLO/spinel composites.

1. Introduction

Li-ion batteries, which currently dominate the market of portable electronic equipment such as mobile phones and laptops, are facing a bottleneck of limited energy density [1–3]. To overcome this restriction, extensive investigations have been devoted on the development of cathode materials with large capacity and high discharge voltage. The composite $xLi_2MnO_3{\cdot}(1-x)LiMO_2$, has lately attracted much attention; because of a promising energy density of $\sim$ 900 Wh kg^{-1} [4–6]. However, it has been found out that $xLi_2MnO_3{\cdot}(1-x)LiMO_2$ suffers from significant voltage decay upon cycling [7]. Thus, $0.5Li_2MnO_3{\cdot}0.5LiMn_{0.5}Ni_{0.5}O_2$ (abbreviated as LLO) with the lowest voltage decay during the cycling has been intensively explored [7].

LLO is usually synthesized by adding more Li (Li:M = 1.5:1, M = Mn, Ni) than that in traditional layered phases (Li:M = 1:1, M = Mn, Ni). The excessive Li occupies 2b octahedral site, forming $LiMn_6$ superstructure in transition metal layer [8,9]. This product, however, is found to be quite sensitive to the synthetic conditions such as temperature, oxygen partial pressure, and cooling rate, all of which would affect the formation of impurity phases [10–14]. According to Li-Mn-Ni ternary phase diagram [15], LLO is located in a single-phase layered region, and is close to the three-phase region (spinel, layered and rock salt phases). Multiphase composites will be obtained when the ratio of Li, Ni and Mn deviates from the stoichiometry of LLO (Li:Mn:Ni = 1.2:0.6:0.2).

The effects of complicated phase constitution within the Li-Mn-Ni system seems to be twofold. Synthesis methods are often required to be well tuned and controlled to circumvent the impurity phases and defects [16,17]. However, the spinel phase can be intentionally introduced to improve the electrochemical properties of LLO [18,19]. For example, LLO synthesized with less Li results in the formation of multiphase products [20,21]. The spinel phase, which is considered as an impurity phase in LLO, however, can improve the rate properties [22]. This result signifies that the complexity of phase constitution within Li-Mn-Ni system should be beneficial, but only if the phase composition is well controlled [23,24]. Substitution of Li^+ on the surface of LLO by protons from HNO_3 [18,25], $(NH_4)_2HPO_4$ [26] or TBAOH [27] can also result in the formation of spinel/LLO composites with superior rate

* Corresponding authors.
E-mail addresses: cy_xu@hit.edu.cn (C.-Y. Xu), gzcao@u.washington.edu (G. Cao).
[1] These authors contributed equally to this work.

http://dx.doi.org/10.1016/j.nanoen.2017.08.054
Received 9 July 2017; Received in revised form 23 August 2017; Accepted 30 August 2017
Available online 01 September 2017

properties. Ionic doping is also found to influence the phase compositions in the Li-Mn-Ni system. Ions, including F^- [28,29], B^{3+} [30] and P^{5+} [31] can facilitate the formation of the spinel phase, yielding LLO/spinel composites with improved rate properties.

In our previous work [32], "Li-rich spinel phase decomposition" was investigated for the synthesis of LLO (L)/spinel (S) composites. Compared with traditional methods such as surface coating, the phase components could be controlled and the interfacial bonding of S and L phase strengthened, resulting in enhanced cyclic and rate performance. However, it was found that, in addition to the S to L phase transition, the side-reaction in which the rock salt (R) phase formed will also affect the cyclic and rate performance of the composites. In this work, a systematic investigation of the possible reactions taking place during the decomposition of the S phase has been carried out, and the phase transitions in the S-L-R system (where S is both Li-rich spinel: S_L and normal spinel: S_N) have been determined. Experimental investigations and density functional theory (DFT) calculations have been combined to understand the thermodynamics and kinetics of the reactions. This information has then been used to control the phase transition. The L/S composite demonstrated a relatively low discharge capacity but high capacity retention at high rate when more S phase remained, while more R phase leads to poor rate and cyclic properties.

2. Experimental section

2.1. Materials synthesis

The LLO/spinel composites were synthesized by a polyol method according to the procedure reported in Ref. [32] The raw chemicals are lithium acetate ($LiAc{\cdot}2H_2O$), manganese acetate tetrahydrate ($Mn(Ac)_2{\cdot}4H_2O$) and nickel acetate tetrahydrate ($Ni(Ac)_2{\cdot}4H_2O$). All chemicals were purchased from Sigma-Aldrich without further purification. In brief, $LiAc{\cdot}2H_2O$, $Mn(Ac)_2{\cdot}4H_2O$ and $Ni(Ac)_2{\cdot}4H_2O$ were mixed in 60 mL glycerol. The molar ratios of Li:Mn:Ni are 1.32:0.6:0.2, ensuring that Li is 10% excessive for the stoichiometric ratio of LLO. The solution was then stirred and heated to 170 °C with a ramping rate of 5 °C/min. After heated for 1 h, the solution was water cooled to room temperature immediately, and then transferred into a glass culture dish. The brown precipitates were collected by solvent evaporation at 125 °C to obtain the precursor. The precursor was ground and then calcined with a ramping rate of 3.5 °C/min, first maintained at 500 °C for 2 h, and then at 700 °C for different durations to achieve the final products. The products were collected and washed several times to remove any residual reactants.

To control LLO/spinel composites with different phase contents, the calcination was conducted at 700 °C for various times, the products calcined for 6, 12 and 18 h are labelled as LT-6, LT-12 and LT-18, respectively.

2.2. Materials characterization

The morphology of the products was characterized by scanning electron microscope (SEM, JSM-7000). XRD characterizations were performed on Rigaku D/max-IIIB X-ray diffraction (XRD), with a voltage of 40 kV and a current of 40 mA, using Cu K_α radiation (λ = 0.15405 nm). X-ray photoelectron spectra were collected using Thermo Fisher Scientific VG Kα Probe spectrometer.

High temperature *in-situ* XRD measurements were carried out on a Rigaku D/max-IIIB X-ray diffraction (XRD) with heating rate of 5 °C/min and scanning rate of 9°/min. The furnace chamber had continuous air flow during the measurements. To avoid gas evolution during the test, the precursor was first heated to 350 °C with a ramping rate of 5 °C/min and held for 20 min. The XRD data were collected every 20 °C over temperature range of 350–820 °C.

2.3. Electrochemical measurements

The cathodes for electrochemistry measurements were made by mixing 75% active materials with 15% super P in N-methyl-2 pyrrolidone (NMP), 10% poly(vinylidene fluoride) (PVDF) was then added into the mixture after 30 min grinding. The slurry was then ground for another 30 min until spread onto Al foil. The foil was heated at 60 °C overnight and then punched into square pieces, the typical cathode loading was 2.0–4.0 mg cm^{-2}. The punched electrodes were heated in a vacuum oven at 110 °C for 10 h before transferred into glovebox. All the electrodes were assembled into CR2016 coin-type cells. Li foils were used as counter electrodes and Celgard 2400 membrane as separator. The electrolyte was purchased from BASF, which is composed of 1 M $LiPF_6$ solution in ethylene carbonate (EC)/dimethyl carbonate (DMC) mixture solution (1:1 by volume). The galvanostatic charge/discharge cycle tests with voltage range from 2.0 to 4.8 V. were carried out with Land CT2001A battery test systems (LAND Wuhan Corp., China). The cyclic voltammetry (CV) and electrochemical impedance spectroscopy (EIS) measurements were carried out on an electrochemical workstation (CHI 660 C, Shanghai Chenhua Instrument Corp., China). The scan rate of CV test was 0.05 mV/s, and the EIS was carried out with AC voltage of 5 mV over the frequency range of 0.01 Hz to 100 kHz.

2.4. Computation methods

All calculations were performed using the Vienna *ab* initio simulation package [33] within projector augmented wave (PAW) framework [34]. The functional for electron exchange and correlation was chosen as GGA with a Hubbard U correction following the rotationally invariant form [35]. The effective U values for the *d*-states of Ni and Mn were set to 6.0 and 3.9 eV based on literature values, respectively [36–40]. Valence electrons were described by a plane wave basis set with an energy cutoff of 520 eV. A Monkhorst-Pack k-point mesh of $4\times4\times4$ was used to sample the Brillouin zone. The superstructure was constructed of 56 atoms containing eight cubic spinel lattice of $LiNi_{0.5}Mn_{1.5}O_4$ units, using an initial configuration from the Materials Project database [39]. All structures were fully relaxed until the force on each atom was less than 0.01 eV/Å.

The structure of disordered $LiNi_{0.5}Mn_{1.5}O_4$ phase (space group: $Fd\bar{3}m$) with uniform Ni/Mn distribution was taken from calculations by Shiiba [40] and Lee [41]. The Li-rich spinel structure was obtained by replacing M (Mn/Ni) with Li in one unit cell, corresponding to $Li_{1.125}M_{1.875}O_4$. All M sites were examined to find the lowest energy configuration. The substitutional formation energy, E^F, was calculated by,

$$E^F = E(Li_{1+x}M_{2-x}O_4) + x\mathrm{E(M)} - E(LiNi_{0.5}Mn_{1.5}O_4) - x\mathrm{E(Li)} \quad (1)$$

where $E(Li_{1+x}M_{2-x}O_4)$ is the total energy of the Li-rich spinel structure, E(M) is the energy of substituted transition metal (Mn or Ni), E($LiNi_{0.5}Mn_{1.5}O_4$) is the total energy of the $Fd\bar{3}m$ $LiNi_{0.5}Mn_{1.5}O_4$, E(Li) is the energy of Li, and x is the amount of excess Li.

Oxygen vacancies were created in both the Li-rich spinel structure and the conventional disordered $Fd\bar{3}m$ $LiNi_{0.5}Mn_{1.5}O_4$ structure. To simplify the calculations, one oxygen vacancy was created in the unit cell, corresponding to a vacancy concentration of 3.125 at%. All 32 of the oxygen sites were examined to find the lowest energy configuration. The oxygen vacancy formation energy E^F was calculated according to

$$E^F = E\left(Li_{1+x'}M_{2-x'}O_{4-\delta}\right) + \delta/2\mathrm{E}(O_2) - E\left(Li_{1+x'}M_{2-x'}O_4\right) \quad (2)$$

where δ is the concentration of oxygen vacancies, $E(Li_{1+x'}M_{2-x'}O_{4-\delta})$ is the total energy of the structure with the oxygen vacancy, E(O_2) is the energy of the O_2 molecule, $E(Li_{1+x'}M_{2-x'}O_4)$ is the total energy of the structure without oxygen vacancies. An energy correction for the O_2 molecules was employed as described by Wang et al. [42]

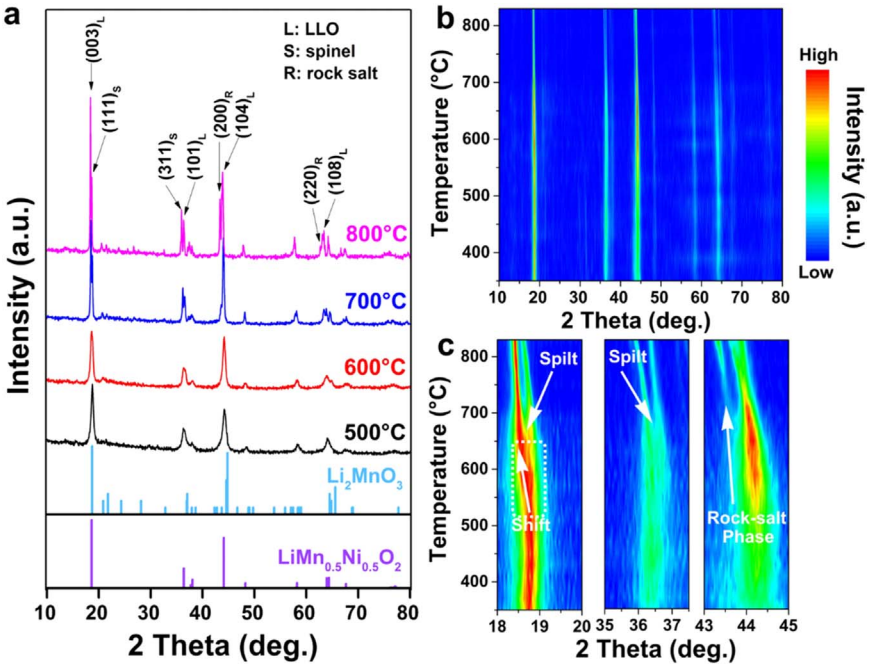

Fig. 1. *In-situ* XRD characterizations to identify the phase transitions in L/S composite during the heating process. (a) XRD patterns of L/S composites obtained at different temperatures. The peaks marked as $(003)_L$, $(101)_L$, $(104)_L$, and $(108)_L$ are reflections of the LLO phase. The peaks marked as $(111)_S$ and $(311)_S$ are reflections of the spinel phase. The peaks marked as $(200)_R$ and $(220)_R$ are reflections of the rock salt phase. (b) Overall *in-situ* XRD pattern from 350–820 °C. (c) Highlighted regions at 18–20°, 35–37.5° and 43–45°. The measurement was taken with a ramping rate of 5 °C/min and the data were collected every 20 °C. Air was flowed throughout the measurement.

3. Results and discussion

3.1. Phase evolution by in/ex-situ XRD studies

In-situ XRD measurements along with Rietveld refinements are always used as the most effective method to explore continuous phase transition process [12,15]. Thus, the *in-situ* XRD patterns (Fig. 1) of products obtained by polyol method were recorded over a temperature range of 350–820 °C, aiming to exam the phase transition during the heating treatment. Fig. 1a presented the *in-situ* XRD patterns obtained at 500, 600, 700 and 800 °C, respectively; demonstrating the coexistence of three phases: S, L and R. The magnified regions between 18–20°, 35–37°, 43–45° and 62–66° are shown in Fig. S1†. The relative diffraction intensities corresponding to the L and R phases increases with temperature, indicating the increased amounts of L and R phases in the composites. Some shoulder peaks appeared when the material was calcined at temperatures above 700 °C (Fig. S1†), which is possibly caused by the formation of Ni-rich or Mn-rich phases within the LLO particles [15]. The overall *in-situ* patterns were presented as contour lines to insure the readability (Fig. 1b).

As previously reported [32], decomposition of the S phase has two pathways: S_L to the L phase and S_N to the R phase (Eqs. (3) and (4)). The relative peak intensities of the S and L phases, S and R phases should be indicative of these phase transitions. Fig. 1c shows the peaks located in the 18–20° and 35–37.5° regions where the diffraction peaks of the S and L phases split [22,43]. The peak in the 18–20° range shifts to a lower angle when calcined at temperatures above 550 °C, presenting an increased amount of the L phase from above 550 °C during the *in-situ* heating process. With further increasing temperatures, the S phase continues decomposing into the L phase, and both the peaks located in 18–20° and 35–37.5° split at temperatures above 670 °C. The R phase is identified by the split shoulder peaks located at 43–45° [15,44]. Fig. 1c reveals that the shoulder peaks at 43.5° emerges when heated above 700 °C, and the increased intensity at high temperature indicates the formation of the R phase. Both the phase transitions from S_L to L (Eq. (3)) and S_N to R (Eq. (4)) would take place at temperature above 500 °C, though the precise phase transition temperature of each reaction could not be identified.

$$\mathrm{Li}_{1+x_1}\mathrm{Ni}_{x_2}\mathrm{Mn}_{2-x_1-x_2}\mathrm{O}_4 + y_1[y_2\mathrm{Li}_2\mathrm{MnO}_3\cdot(1-y_2)\mathrm{LiNi}_{0.5}\mathrm{Mn}_{0.5}\mathrm{O}_2] \leftrightarrow (1-z)\mathrm{Li}_{1+x'}\mathrm{Ni}_{x_3}\mathrm{Mn}_{2-x'-x_3}\mathrm{O}_4 + y_1'[y_2'\mathrm{Li}_2\mathrm{MnO}_3 \cdot(1-y_2')\mathrm{LiNi}_{0.5}\mathrm{Mn}_{0.5}\mathrm{O}_2] + z/2\mathrm{O}_2 \quad (3)$$

where $x' = (x-z)/(1-z)$, $x_3 = x_2/(1-z)$, $y_1' = y_1 + z$ and $y_2' = (z + y_1y_2)/(y_1 + z)$

$$LiNi_{0.5}Mn_{1.5}O_4 \leftrightarrow \alpha Li_xNi_{1-x}O + \beta LiNi_{0.5-y}Mn_{1.5+y}O_4 + \gamma O_2 \quad (4)$$

It is worth mentioning that the phase constitution during the *in-situ* test is different from that in our previous work [32] when calcined at the same temperatures. To determine the influence of calcination time, *ex-situ* XRD measurements with short calcination duration (5 min) were carried out at temperatures ranging from 500 to 800 °C. The samples were calcined at given temperatures for 5 min and cooled at 2.5 °C/min. Fig. S2† compares all the *in-situ* (obtained at high temperature without continuous calcination) and *ex-situ* XRD (obtained at room temperature and heated for 5 min: Ex-5m and 12 h: Ex-12h, respectively) patterns of samples calcinated at 500–800 °C. The relative peak intensity of the S and L phases changed little at temperatures below 600 °C with varied heating duration, but for the samples calcined at 700 °C, a prolonged heating time reduced the content of the S phase. The pattern of Ex-5 m sample obtained at 800 °C consists only of L and R phases, indicating that the S phase decomposed completely (Fig. S2d†). In contrast, in the Ex-12 h sample obtained at 800 °C, the S phase reappeared, possibly due to the loss of Li through volatilization [10]. The effect of Li volatilization is neglectable for samples with short calcination durations but might be evident if the calcination duration at 800 °C is as long as 12 h. Thus, the S to L phase transition takes the longest time at 700 °C and reacts completely at 800 °C.

The formation of the R phase is complicated. The corresponding diffraction peaks could not be detected until heated to 700 °C during the *in-situ* test. However, they are found in the pattern of Ex-5m sample at low temperatures (≤ 600 °C) but disappeared again in the pattern of Ex-12h samples at the same temperature. Such results suggest that the R phase could also be leached out from the S phase when the calcination temperature is below 600 °C. However, prolongation the calcination duration to 12 h might lead to another phase transition from the R to S or L phase. According to the phase diagram of Li-Mn-Ni system [15], the R phase can transform into the L phase with increased Li content.

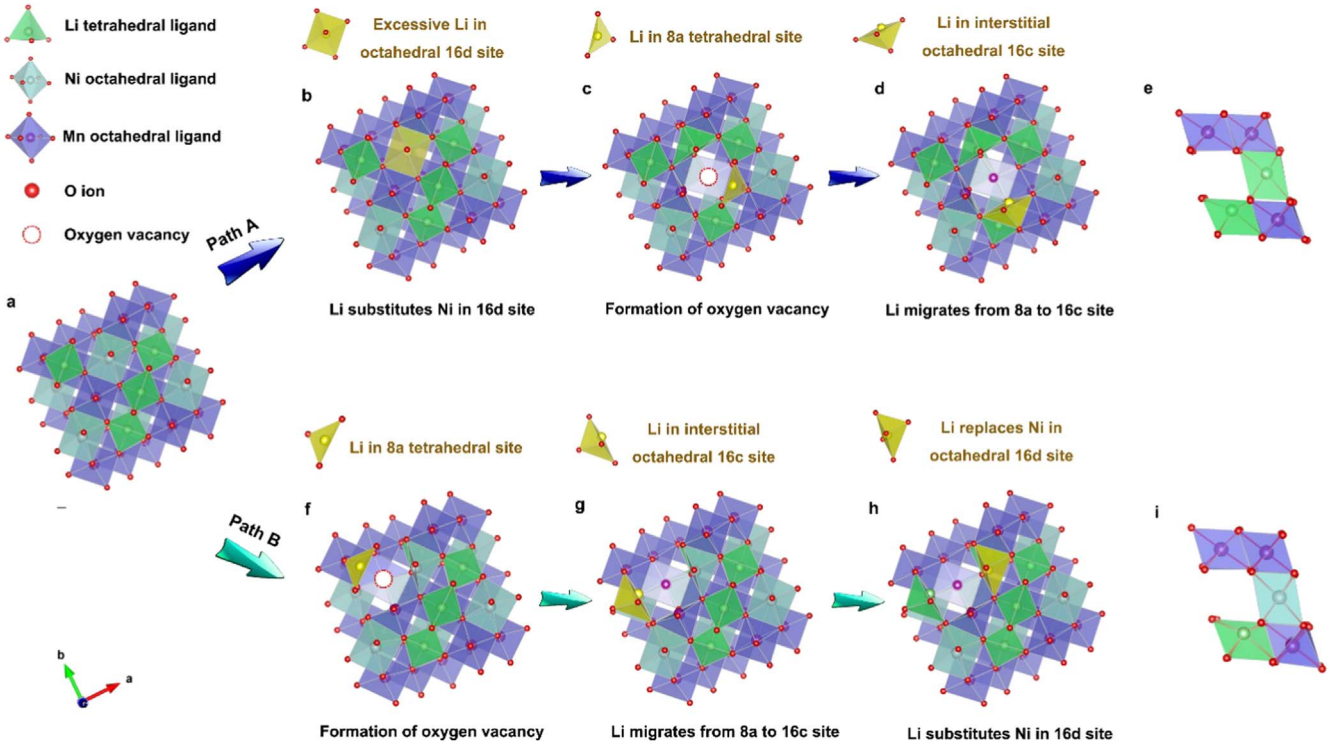

Fig. 2. Intermediates and transition states of two reaction paths from S to quasi-Li_2MnO_3 and quasi-rock salt crystal. Path A: formation of quasi-Li_2MnO_3 crystal in Li-rich spinel phase; Path B: formation of quasi-rock salt crystal and quasi-Li_2MnO_3 crystal in normal $LiNi_{0.5}Mn_{1.5}O_4$. States: (a) Normal $LiNi_{0.5}Mn_{1.5}O_4$ (space group: $Fd\bar{3}m$); (b) Li-rich $Li_{1+x1}Ni_{x2}Mn_{2-x1-x2}O_4$; (c) Li-rich $Li_{1+x1}Ni_{x2}Mn_{2-x1-x2}O_{4-\delta}$ with oxygen vacancy; (d) Li-rich $Li_{1+x1}Ni_{x2}Mn_{2-x1-x2}O_{4-\delta}$ with quasi-Li_2MnO_3 crystal; (e) quasi-Li_2MnO_3 crystal; (f) $LiNi_{0.5}Mn_{1.5}O_{4-\delta}$ with oxygen vacancy; (g) $LiNi_{0.5}Mn_{1.5}O_{4-\delta}$ with quasi-rock salt crystal; (h) $LiNi_{0.5}Mn_{1.5}O_{4-\delta}$ with quasi-Li_2MnO_3 crystal; (i) quasi-rock salt crystal. Noted that some of these transition states could not been stable in normal condition.

Thus, given the excess Li in the precursor, the R phase which leached from the S phase would likely transform into the L phase given sufficient reaction time. The decreased content of the R phase in the Ex-5m and Ex-12h samples obtained at 700 and 800 °C also indicates the phase transition from the R to L phase.

3.2. DFT calculations and structure evolution mechanism

For better understanding of the phase evolution, DFT calculations were performed to investigate the structure evolution in the S_L and S_N phases (space group: $Fd\bar{3}m$). According to Eqs. (3) and (4), both phase transitions involve oxygen evolution, suggesting the formation of oxygen vacancies in the S_L and S_N crystals during the phase transitions. Oxygen vacancies have been found to promote the migration of cations and lead to phase transition in LLO [45]. In this work, the essence of such phase transitions may be associated with cation migration in the S_L and S_N phases.

The excess Li in the S_L phase has been considered to substitute transition metals [46–49], so the S_L structure was constructed by replacing M (Mn, Ni) with Li, corresponding to the stoichiometry $Li_{1.125}M_{1.875}O_4$. The configuration with the lowest energy is obtained when one Ni located in a 16d octahedral site is replaced by Li (Fig. 2b), corresponding to the stoichiometry $Li_{1.125}Ni_{0.325}Mn_{1.5}O_4$. An oxygen vacancy is created on both S_L and S_N, resulting in a vacancy concentration of 3.125 at%. As shown in Fig. 2c, the oxygen vacancy is formed near the excess Li in the S_L crystal, and the oxygen vacancy in S_N (Fig. 2f) is formed on oxygen sites which coordinated with 1 Li, 1 Ni and 2 Mn ions. Note that in both the S_L and S_N structures, the oxygen vacancy would break the nearby tetrahedral ligand of coordinated Li located in the 8a site. Therefore, these Li ions appears to be able to migrate to nearby interstices. As mentioned by Thackeray [47], the S phase could transfer into a layered structure when the interstitial 16c octahedral sites in the transition metal layer are occupied by Li. For the S_L structure considered here, the migration of Li from an 8a tetrahedral site to an interstitial 16c octahedral site in the transition metal layer result in the formation of a quasi-Li_2MnO_3 crystal, as shown in Fig. 2d. The local version of the quasi-Li_2MnO_3 crystal is shown in Fig. 2e, where one layer is composed of Li, Mn, Ni octahedral ligands and the other one composed of Li octahedral ligand. It has been suggested that this kind of quasi layer crystal would lead to further oxygen rearrangement to accommodate the extra lithium [47]. Therefore, the quasi-Li_2MnO_3 crystal would possibly transform into the L phase with excessive Li (Fig. S3†). However, for the S_N phase, the structure in which Li migrated from an 8a tetrahedral site to an octahedral site (Fig. 2g) is more likely to form a quasi-rock salt crystal. In the quasi-rock salt crystal (Fig. 2i), Li, Mn and Ni are arranged in octahedral sites in the transition metal layer, while Ni is arranged in the octahedral site of Li layer. As demonstrated in Fig. 2h, such quasi-rock salt crystal could transform into quasi-Li_2MnO_3 crystal if additional Li were to replace Ni in the octahedral 16d site of the Li layer.

Fig. 3 shows the free energy change for each step along path A and B schematically depicted in Fig. 2. The energy change was calculated following equations analogous to Eqs. (1) and (2). The formation energy of an oxygen vacancy in the S_L structure (1.85 eV) is lower than that in S_N (2.39 eV), indicating that oxygen vacancy formation is more likely in the S_L structure. The formation energy of quasi-Li_2MnO_3 crystal is 0.2 eV in the S_L structure (Fig. 3a), corresponding to 3.64 meV per atom. This value is much smaller than the thermal energy at 300 K (75 meV per atom) [40], suggesting this structural evolution is thermodynamically favorable at room temperature. As shown in Fig. 3b, the formation energy of the quasi-rock salt crystal is 0.31 eV, corresponding to 5.6 meV per atom. Therefore, both of these two structural evolutions are thermodynamically favorable, and the formation of the quasi-Li_2MnO_3 crystal in the S_L phase is favored thermodynamically. The energy difference of the structural evolution from the quasi-rock salt to quasi-Li_2MnO_3 crystal in Fig. 3b is −4.61 eV, indicating that this phase

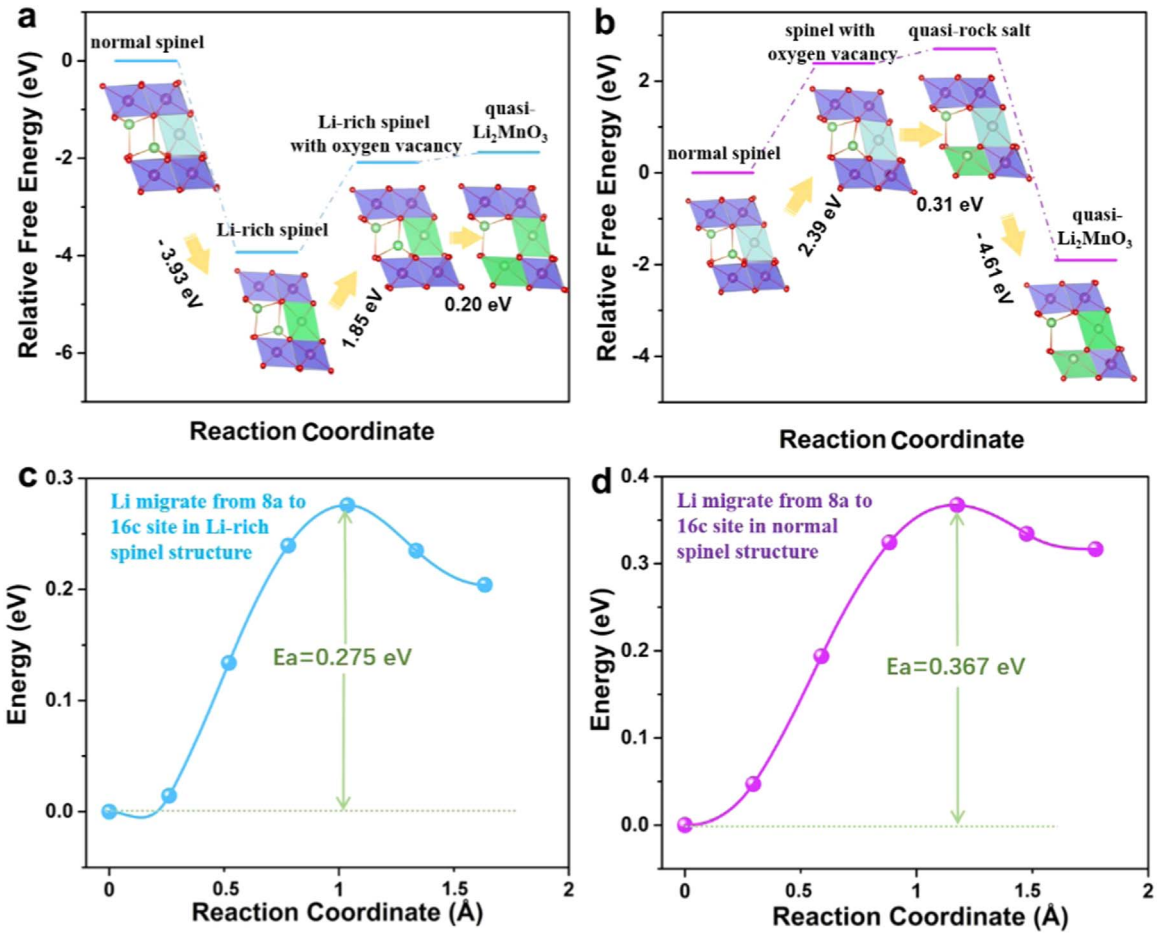

Fig. 3. Calculated free energy diagrams of the following reactions. (a) normal spinel→Li-rich spinel→Li-rich spinel with oxygen vacancy→quasi-Li_2MnO_3 crystal; (b) normal spinel→spinel with oxygen vacancy→quasi-rock salt crystal→quasi-Li_2MnO_3 crystal, and the minimum energy pathways of Li migration from a tetrahedral 8a site to an interstitial octahedral 16c sites in (c) Li-rich spinel structure with oxygen vacancy; (d) normal spinel structure with oxygen vacancy.

transition is also thermodynamically favored. The migration barriers of Li from an 8a tetrahedral site to an 16c octahedral site in both S_L and S_N structure were shown in Fig. 3c and d, respectively. The Li diffusion barrier is 0.275 eV for the S_L structure and 0.367 eV for the S_N structure, indicating that the formation of quasi-Li_2MnO_3 crystal in S_L structure is more likely than the formation of quasi-rock salt crystal in S_N structure. These calculations indicate that both structural evolutions could take place reversibly, which is in accordance with Eqs. (1) and (2). However, as illustrated in Gao's research [46], the reversibility is associated with the content of excessive Li; as a consequence, the S_L would transform into the L structure irreversibly when Li is in excess.

The phase transition from S_L to L and S_N to R is depicted as follows: (1) the formation of an oxygen vacancy; (2) the migration of Li near the oxygen vacancy from an 8a tetrahedral site to an interstitial 16c octahedral site, forming a quasi-Li_2MnO_3 crystal and quasi-rock salt crystal in S_L and S_N, respectively; and (3) oxygen ion rearrangement to accommodate excess lithium ions. The phase transition from R to L is initiated by the substitution of Ni by additional Li.

A schematic diagram of the entire phase transition (Scheme 1) can be summarized based on our experimental and theoretical study. Based on our DFT calculations, both the formation energies of oxygen vacancies and the quasi-Li_2MnO_3 crystal in the S_L structure is favorable as compared to the formation of oxygen vacancies and the quasi-rock salt crystal in the S_N structure. Therefore, the formation of the quasi-Li_2MnO_3 crystal in the S_L phase is thermodynamically favorable over the formation of the quasi-rock salt crystal in S_N. The low formation energy (−4.61 eV) of the quasi-Li_2MnO_3 crystal from quasi-rock salt crystal suggests that this reaction has the highest driving force, if excess Li is present.

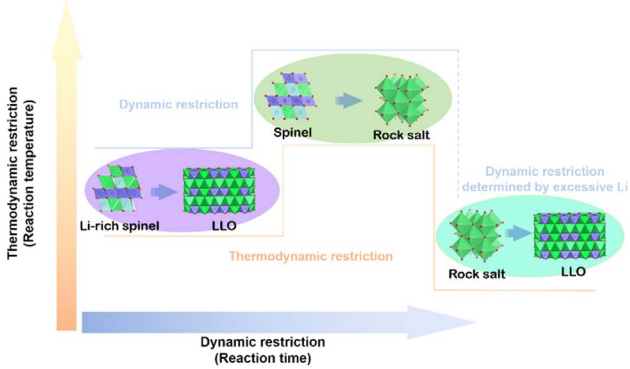

Scheme 1. Schematic diagram of the thermodynamic and dynamic kinetic driving force for the phase transitions. From Li-rich spinel phase to LLO, normal spinel phase to rock salt phase and rock salt phase to LLO.

The dynamic of each reaction was compared from the XRD patterns at low temperatures (≤ 600 °C). As the L phase did not change much in the patterns of *in-situ*, Ex-5m and Ex-12h samples, the phase transition from S_L to L phase appear to be almost finished immediately at target temperatures. In comparison, the R phase appeared only in Ex-5m patterns at low temperatures (≤ 600 °C), suggesting that the reaction requires more time for completion at these temperatures. So, the S_L to L phase transition is kinetically favored over the phase transition from the S_N to the R phase, in agreement with the calculations. Note that the reaction kinetics of the phase transition from R to L phase is dependent on the content of excess Li.

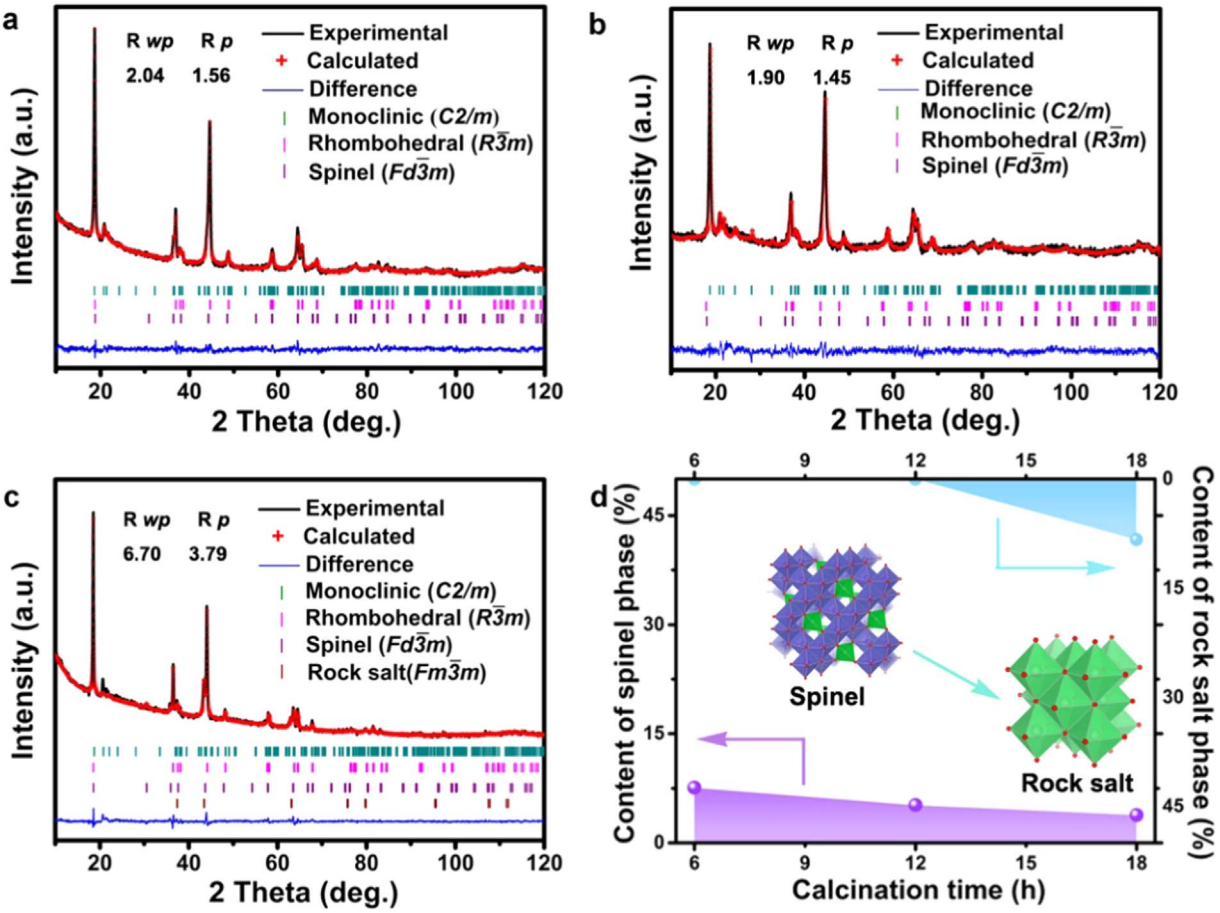

Fig. 4. Powder XRD patterns (black lines) and a Rietveld fit (red plus sign) for products calcined at 700 °C in air over different time durations. (a) 6 h; (b) 12 h and (c) 18 h. The refinement was carried out using the monoclinic *C2/m* space group (dark cyan vertical tick marks), rhombohedral $R\bar{3}m$ space group (pink vertical tick marks), spinel $Fd\bar{3}m$ space group (purple vertical tick marks) and rock salt $Fm\bar{3}m$ space group (wine vertical tick marks); the blue line is the difference between the observed and calculated patterns. (d) Rietveld refinement content of the spinel phase in the products calcined at different temperatures in air for 12 h. The crystal structures of $LiNi_xMn_{2-x}O_4$ and $Li_xNi_{1-x}O$ are shown as insets in (d).

3.3. Design of a LLO/spinel nanocomposite by accommodating the phase transition

3.3.1. Morphology and crystal structure

The morphologies of samples calcined at 700 °C for 6 h (LT-6), 12 h (LT-12)and 18 h (LT-18) are shown in Fig. S4†. Both the particle size and the polyhedral characteristic have no prominent change, suggesting the duration time at 700 °C had little influence on the morphology. The tap densities of LT-6, LT-12 and LT-18 are 1.63 g cm^{-3}, 1.68 g cm^{-3} and 1.59 g cm^{-3} respectively.

The XRD patterns and Rietveld refinements of LT-6, LT-12 and LT-18 are shown in Fig. 4a-c. As described previously, the three phases that could have formed during the calcination process are: the L phase with the combined pattern of monoclinic cell (*C2/m* Li_2MnO_3) and rhombohedral cell ($R\bar{3}m$ $LiNi_{0.5}Mn_{0.5}O_2$) [45], the S phase with the pattern of cubic cell ($Fd\bar{3}m$ $LiNi_xMn_{2-x}O_4$) and the R phase with the pattern of cubic cell ($Fm\bar{3}m$ $Li_xNi_{1-x}O$). From our preliminary analysis of the XRD pattern, the phase compositions in LT-6 and LT-12 were assumed to be a mixture of L and S, while the phase composition in LT-18 was assumed to be a mixture of L, S and R. Detailed refinement results are listed in Table 1, where the lattice parameters were simplified using the space group of $R\bar{3}m$ with a higher symmetry [50]. There appears to have been a slight increment of both the *a* and *c* values correlated with a prolonged calcination time, which is in accordance with the shift of reflections towards lower angles. As described by Wang et al. [10] a prolonged calcination time may give rise to the volatilization of lithium and consequently the reduction of Mn^{4+} ions (0.53 Å) to larger Mn^{3+} ions (0.58 Å). Additionally, the intensity ratio of $I_{(003)}/I_{(104)}$, which is considered to be an indication of Li^+/Ni^{2+} antisite defect [51], is slightly higher in LT-18; suggesting the suppression of antisite defects with a longer calcination time.

Table 1
Detailed XRD Rietveld refined results of each product calcined at 700 °C in air as a function of calcination time.

Samples	Lattice parameter (Å)		$I_{(003)}/I_{(104)}$	Ni^{2+}% ($Ni_{3b}^{2+}/Ni_{total}^{2+}$)
	a_{hex}	c_{hex}		
LT-6	2.8541	14.2407	1.4	3.4
LT-12	2.8758	14.2531	1.2	5.5
LT-18	2.8874	14.3869	1.6	2.1

The contents of the S and R phases in each sample are shown in Fig. 4d. LT-6 has the highest S content with a mass fraction of 7.6%, and that content gradually decreased to 5.2% in LT-12 and then 3.8% in LT-18. Thus, an increased calcination time at 700 °C promotes the S to L transition. It should be mentioned that in the XRD pattern of LT-18, the peaks indexed to the R phase become distinguishable. As mentioned before, the phase transition from R to L phase is thermodynamically favorable at 700 °C, but restricted by the Li content. Therefore, the R phase in LT-18 suggests that Li may be gradually volatilized within the 18 h heating.

3.4. Surface composition analyses

High-resolution XPS spectra and the fitted curves of Mn 3s and Ni

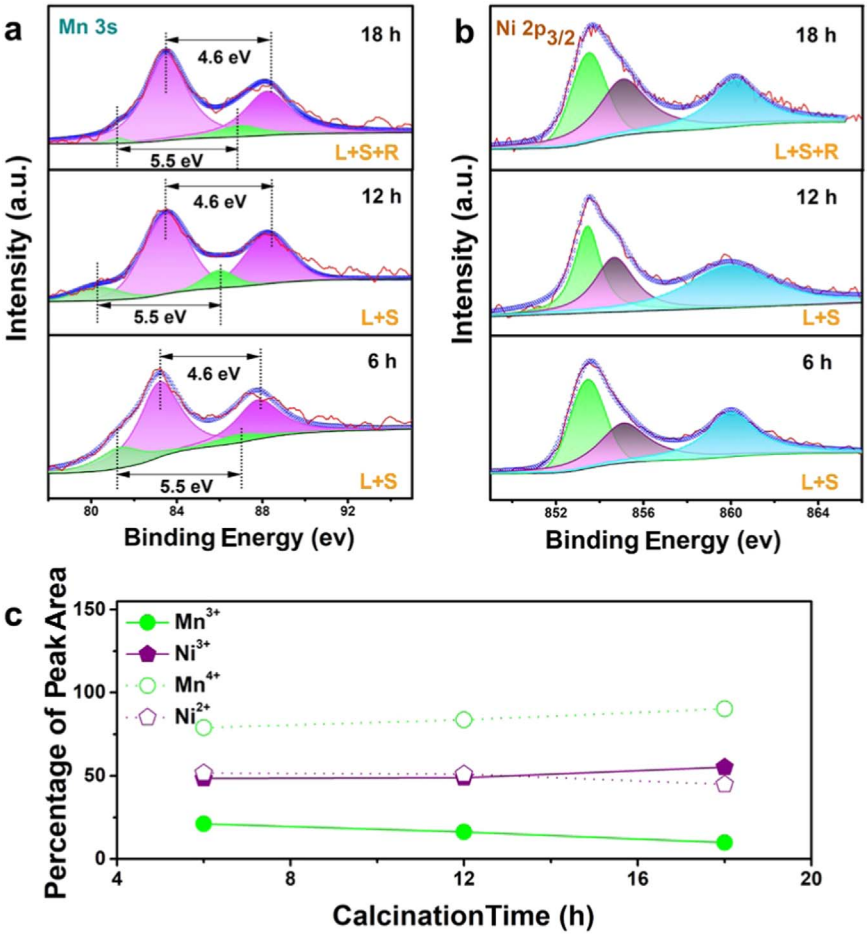

Fig. 5. (a) Mn 3s and (b) Ni $2p_{3/2}$ XPS spectra of products calcined at 700 °C in air for different times. (c) Percentage of fitted peak area. The differentiated and fitted peaks are shown in different colours.

$2p_{3/2}$ are shown in Fig. 5a and b, with the percentage of the fitted peak area shown in Fig. 5c. It is worth mentioning that the oxidation states of the transition metals are different in the L and S phases. The valence of transition metals is widely considered to be Mn^{4+} and Ni^{2+} in the pure L phase [29,52], while the oxidation states of transition metals in S phase are depended on the content of Ni; $LiNi_{0.5}Mn_{1.5}O_4$ presents the same oxidation states in the L phase, but Mn tends to exist as both Mn^{3+} and Mn^{4+} when the content of Ni is below 0.5 per formula unit [53]. Additionally, the decomposition reaction (Eq. (4)) of S would also introduce a Ni^{3+} species [54].

The Mn 3s spectra has been differentiated based on the fact that each valence state of Mn has two multiplet split components with different splitting energies: the splitting energy of Mn^{3+} is 5.5 eV, and Mn^{4+} is 4.6 eV [55]. For the Ni $2p_{3/2}$ spectra in Fig. 5b, the peak located near 854 eV is attributed to Ni^{2+}, while the one at 855 eV is Ni^{3+} [56]. According to the comparison of peak area in Fig. 5c, the amount of Mn^{3+} in LT-6 is higher than in LT-12 and LT-18, and the amount of Ni^{3+} in LT-18 is higher than in LT-6 and LT-12. This trend is in agreement with the XRD results that LT6 has more S phase and LT-18 has more R phase. The O1s spectra of all the three samples (Fig. S5†) were almost the same, indicating the oxidation state of oxygen on the surface has not been affected by the calcination time.

3.5. Electrochemical properties

Li metal half cells were assembled with all the samples, SEM images of the prepared electrodes shown in Fig. S6† suggested the homogeneous mixture of active materials with super P. The electrochemical properties of the calcination time-resolved samples were compared and the results are shown in Fig. 6. When cycled between 2 and 4.8 V with the current density of 20 mA g^{-1} (0.1 C, 1 C = 200 mA g^{-1}), LT-12 presents the highest discharge capacity of 218 mA h g^{-1} in the first cycle, and the discharge capacity of LT-6 and LT-18 is 209 and 171 mA h g^{-1}, respectively (Fig. 6a). In the initial discharge profiles of LT-6, two plateaus corresponding to the redox reaction of the S phase emerge at 2.8 and 4.7 V, which are attributed to the $Li[Ni_{0.5}Mn_{1.5}]O_4$ - $Li_2[Ni_{0.5}Mn_{1.5}]O_4$ transition and Ni^{2+}/Ni^{4+} oxidation reaction, respectively [20]. It has been revealed that the steadiness of these reactions is significantly determined by the crystallinity of the S phase [32]; plateaus in samples calcined below 700 °C decayed rapidly in the first five cycles. As shown in Fig. S7†, such redox reactions of LT-6 are stable within the first five cycles, suggesting a higher crystallinity of the S phase. The plateaus of the S phase almost vanished in the charge-discharge profile of LT-12 and LT-18, consistent with a reduced content of the S phase in the two composites. In the 5th cycle, all the samples had higher discharge capacities than in the first cycle, which is caused by suppression of Li_2MnO_3 activation process in the first several cycles [57].

The cyclic voltammetry measurements shown in Fig. 6b displayed and compared the redox reaction in the first three cycles of the samples. Three pairs of redox peaks marked by dash purple cycles are indicative of the redox reactions of S phase, corresponding to the plateaus at 2.8 and 4.7 V in the discharge curves of Fig. 6a. In accordance with the phase constitution change, the relative intensity of peaks attributed to the S phase diminished with a prolonged calcination time. Meanwhile, in the first cycle, peaks referred to Ni^{2+}/Ni^{3+} and Ni^{3+}/Ni^{4+} redox reactions between 4.6–4.8 V overlap with the activation peak of LLO. Therefore, curves of LT-12 and LT-18 with higher L content, the peaks are broadened and merged together. The wide cathodic peak located around 3.3 V is attributed to the reversible $Mn^{4+} \rightarrow Mn^{3+}$ reduction process in the L phase [58].

In the results of the rate properties shown in Fig. 6c, LT-12

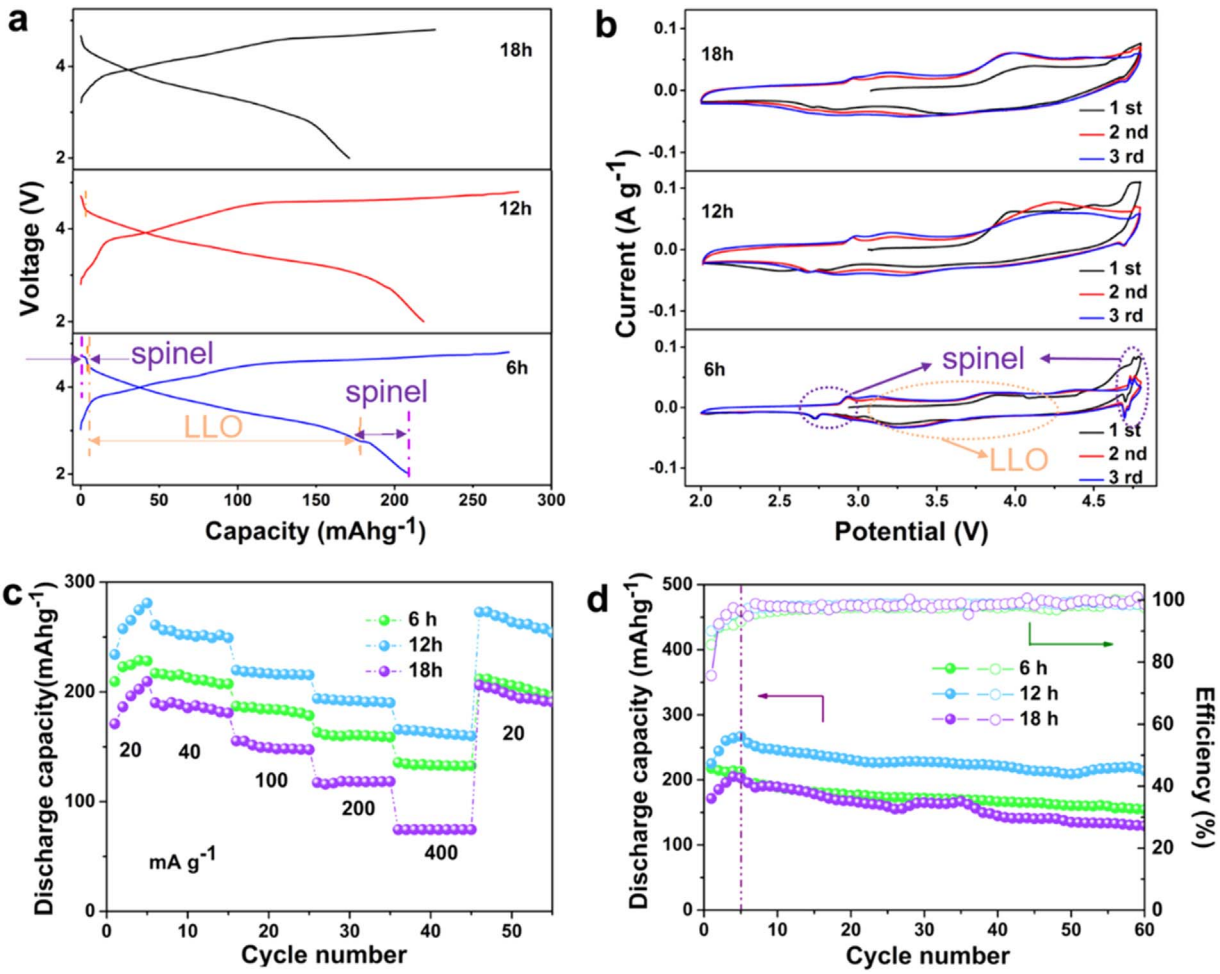

Fig. 6. Electrochemical properties of products calcined at 700 °C in air for different time. (a) First charge-discharge profiles at 0.1 C rate (1 C = 200 mA g^{-1}), (b) the first three cycles cyclic voltammograms, (c) rate and (d) cyclic properties capability.

presented the highest capacity during each rate, the discharge capacity is 166 mA h g^{-1} at 2 C (400 mA g^{-1}) which is better than many previous reports [10,59–61]. Although the discharge capacity of LT-6 is not as high as that in LT-12, the capacity retention at high rates is higher than LT-12. When the rate increased from 0.1 to 2 C, the capacity retention is 63% for LT-6 and 58% for LT-12, suggesting a large S content could improve the rate performance. The rate performance of LT-18 is not as good as LT-6 and LT-12, which may be affected by the increased content of the R phase [10]. Cycling tests were carried out at room temperature, the rate is 0.2 C with the first five activation cycles at 0.1 C. As shown in Fig. 6d, the capacity retention is 79%, 83% and 68% after 60 cycles at 0.2 C for LT-6, LT-12 and LT-18, respectively. The cyclic property of LT-6 is slightly lower than that of LT-12, which is possibly associated with the higher lattice strains caused by the lattice parameter difference of the S and L phases [27]. It should be noted that the cycling profiles of LT-6 and LT-18 are overlapped in the first 15 cycles, which may be caused by two aspects: 1. The discharge capacities of LT-6 and LT-18 are relative close at low rate, so deviations caused by technical factors may lead to the floating of capacity. 2. S phase is more beneficial to the rate property, but upon short term cycling, the capacity decay caused by lattice strains is comparable with that of R phase.

It should be noted that as L phase would gradually transform into S and R phases during long term cycling [62], so the electrochemical properties of the L/S composites would possibly influenced by that in-operando phase transitions. To have qualitative comparison of that effect, the 1st and 50th discharge curves with normalized capacities were shown in Fig. S8†. For the 1st cycle, the normalized capacities in 4.5–4.8 V and 2.0–2.75 V of the L/S composites were calculated to qualitative compare the contents of spinel phase; for the 50st cycle, the normalized capacities from the inflection points (shown in the inset of Fig. S8b†) to 2.0 V were calculated to qualitative compare the contents of spinel phase. Noted that LT-18 has slightly higher normalized capacity of spinel phase than LT-12, which is more likely to be caused by the larger polarization on the basis of the discharge profiles. After 50 cycles, the increments of the normalized capacities of spinel phase are 0.583, 0.581 and 0.589 for LT-6, LT-12 and LT-18, respectively, suggesting the contents of in-operando formed spinel phase are almost the same in the three samples upon cycling. Therefore, the influence of in-operando formed rock salt and spinel phase seems to be comparable in all the three samples.

Fig. S9† displayed the Nyquist plots of the electrodes made by products calcined at 700 °C for different times. Prior to the measurements, all the cells were charged to 4.2 V after 3 cycles of charge-discharge to ensure identical status. The equivalent circuit was simulated by Z-view software and shown in the insert of Fig. S9†. The values of simulated R_s and R_{ct} of all the samples were listed in Table 2. From that results, the resistances of LT-6 and LT-12 seems to be comparable but the surface resistance(R_s) in LT-18 is much higher than the others, which is possibly associated with the different heterostructures at the interface.

Table 2
Values of R_s, R_{ct} of products calcined at 700 °C in air for different time after 3 cycles at 0.1 C and 25 °C.

	LT-6	LT-12	LT-18
$R_s(\Omega)$	20.8	16.9	51.4
$R_{ct}(\Omega)$	143.7	156.2	161.0

4. Conclusions

Three kinds of phase transitions in $xLi_2MnO_3{\cdot}(1-x)LiMO_2$ (LLO)/spinel composites have been found out, that are: S_L to L, S_N to R and R to L. DFT calculations of the structural evolution revealed that the release of oxygen from the S_L and S_N structures promote the formation of quasi-Li_2MnO_3 and quasi-rock salt crystals. The phase transition from S_L to L have higher thermodynamic and dynamic driving forces than the phase transition from S_N to R, and the phase transition from R to L is energetically favorable once excess Li is provided. The reaction priority has been utilized to design LLO/spinel composites with different phase constitutions, in which the calcination time was controlled to influence the content of each reaction. The obtained composite with a moderate amount of S phase showed good cycling and rate performance, composite with more S phase demonstrated lower discharge capacity but higher capacity retention at high rates. Prolonged time would lead to the formation of the R phase, which resulted in poor electrochemical properties.

Acknowledgements

This work was financially supported in part by the National Science Foundation (DMR 1505902). Y.P, and Q.C. would like to thank the China Scholarship Council (CSC) for supporting their study as exchanging students in U.W. and UT Austin. The authors gratefully acknowledge Dr. Xi-Ping Cui for XRD measurements and Fei Huang for SEM measurements.

Appendix A. Supplementary material

Supplementary data associated with this article can be found in the online version at http://dx.doi.org/10.1016/j.nanoen.2017.08.054.

References

[1] J.B. Goodenough, Energy Environ. Sci. 7 (2014) 14–18.
[2] V. Etacheri, R. Marom, R. Elazari, G. Salitra, D. Aurbach, Energy Environ. Sci. 4 (2011) 3243.
[3] R.C. Massé, E. Uchaker, G. Cao, Sci. China Mater. 58 (2015) 715–766.
[4] B.C. Melot, J.M. Tarascon, Acc. Chem. Res. 46 (2013) 1226–1238.
[5] C. Liu, Z.G. Neale, G. Cao, Mater. Today 19 (2015) 109–123.
[6] K. Zhang, Z. Hu, Z. Tao, J. Chen, Sci. China Mater. 57 (2014) 42–58.
[7] J. Wang, X. He, E. Paillard, N. Laszczynski, J. Li, S. Passerini, Adv. Energy Mater. 6 (2016) 1600906.
[8] W. Liu, P. Oh, X. Liu, S. Myeong, W. Cho, J. Cho, Adv. Energy Mater. 5 (2015) 1500274.
[9] R.Z. Yu, X.Y. Wang, Y.Q. Fu, L.W. Wang, S.Y. Cai, M. Liu, B. Lu, G. Wang, D. Wang, Q.F. Ren, X.K. Yang, J. Mater. Chem. A. 4 (2016) 4941–4951.
[10] C.-C. Wang, K.A. Jarvis, P.J. Ferreira, A. Manthiram, Chem. Mater. 25 (2013) 3267–3275.
[11] R. Shunmugasundaram, R. Senthil Arumugam, J.R. Dahn, Chem. Mater. 27 (2015) 757–767.
[12] J. Li, J. Camardese, S. Glazier, J.R. Dahn, Chem. Mater. 26 (2014) 7059–7066.
[13] C. Jacob, J. Jian, Q. Su, S. Verkhoturov, R. Guillemette, H. Wang, ACS Appl. Mater. Interfaces 7 (2015) 2433–2438.
[14] A. Manthiram, J.C. Knight, S.-T. Myung, S.-M. Oh, Y.-K. Sun, Adv. Energy Mater. 6 (2016) 1501010.
[15] E. McCalla, A.W. Rowe, R. Shunmugasundaram, J.R. Dahn, Chem. Mater. 25 (2013) 989–999.
[16] J. Ma, B. Li, L. An, H. Wei, X. Wang, P. Yu, D. Xia, J. Power Sources 277 (2015) 393–402.
[17] M. Chen, X. Xiang, D. Chen, Y. Liao, Q. Huang, W. Li, J. Power Sources 279 (2015) 197–204.
[18] S.H. Kang, C.S. Johnson, J.T. Vaughey, K. Amine, M.M. Thackeray, J. Electrochem. Soc. 6 (2006) A1186–A1192.
[19] M. Chen, D. Chen, Y. Liao, X. Zhong, W. Li, Y. Zhang, ACS Appl. Mater. Interfaces 8 (2016) 4575–4584.
[20] S. Park, S. Kang, C. Johnson, K. Amine, M. Thackeray, Electrochem. Comm. 9 (2007) 262–268.
[21] J. Cabana, S.H. Kang, C.S. Johnson, M.M. Thackeray, C.P. Grey, J. Electrochem. Soc. 156 (2009) A730–A736.
[22] D. Luo, G. Li, C. Fu, J. Zheng, J. Fan, Q. Li, L. Li, Adv. Energy Mater. 4 (2014) 1400062.
[23] W. Wei, L. Chen, A. Pan, D.G. Ivey, Nano Energy 30 (2016) 580–602.
[24] W. Li, B. Song, A. Manthiram, Chem. Soc. Rev. 46 (2017) 3006–3059.
[25] C.S. Johnson, N. Li, C. Lefief, J.T. Vaughey, M.M. Thackeray, Chem. Mater. 20 (2008) 6095–6106.
[26] F. Cheng, J. Chen, H. Zhou, A. Manthiram, J. Electrochem. Soc. 10 (2013) A1661–A1667.
[27] J. Zhao, R. Huang, W. Gao, J.-M. Zuo, X.F. Zhang, S.T. Misture, Y. Chen, J.V. Lockard, B. Zhang, S. Guo, M.R. Khoshi, K. Dooley, H. He, Y. Wang, Adv. Energy Mater. 5 (2015) 1401937.
[28] Y.C. Jin, J.G. Duh, ACS Appl. Mater. Interfaces 8 (2016) 3883–3891.
[29] H. Liu, D. Qian, M.G. Verde, M. Zhang, L. Baggetto, K. An, Y. Chen, K.J. Carroll, D. Lau, M. Chi, G.M. Veith, Y.S. Meng, ACS Appl. Mater. Interfaces 7 (2015) 19189–19200.
[30] J. Liu, S. Wang, Z. Ding, R. Zhou, Q. Xia, J. Zhang, L. Chen, W. Wei, P. Wang, ACS Appl. Mater. Interfaces 8 (2016) 18008–18017.
[31] Y. Zhao, J. Liu, S. Wang, R. Ji, Q. Xia, Z. Ding, W. Wei, Y. Liu, P. Wang, D.G. Ivey, Adv. Funct. Mater. 26 (2016) 4760–4767.
[32] Y. Pei, C.-Y. Xu, Y.-C. Xiao, Q. Chen, B. Huang, B. Li, S. Li, L. Zhen, G. Cao, Adv. Funct. Mater. 27 (2017) 1604349.
[33] W. Kohn, A.D. Becke, R.G. Parr, J. Phys. Chem. 100 (1996) 12974–12980.
[34] P.E. Blochl, Phys. Rev. B. 24 (1994) 17953–17979.
[35] A.I. Liechtenstein, Phys. Rev. B. 8 (1995) R5467–R5470.
[36] A. Jain, G. Hautier, S.P. Ong, C.J. Moore, C.C. Fischer, K.A. Persson, G. Ceder, Phys. Rev. B. 84 (2011) 045115.
[37] T. Mueller, G. Hautier, A. Jain, G. Ceder, Chem. Mater. 23 (2011) 3854–3862.
[38] G. Hautier, S.P. Ong, A. Jain, C.J. Moore, G. Ceder, Phys. Rev. B. 85 (2012) 155208.
[39] S.P. Ong, W.D. Richards, A. Jain, G. Hautier, M. Kocher, S. Cholia, D. Gunter, V.L. Chevrier, K.A. Persson, G. Ceder, Comp. Mater. Sci. 68 (2013) 314–319.
[40] H. Shiiba, N. Zettsu, M. Nakayama, S. Oishi, K. Teshima, J. Phys. Chem. C 119 (2015) 9117–9124.
[41] E. Lee, K.A. Persson, Energy Environ. Sci. 5 (2012) 6047–6051.
[42] L. Wang, T. Maxisch, G. Ceder, Phys. Rev. B. 73 (2006) 195107.
[43] D. Wang, R. Yu, X. Wang, L. Ge, X. Yang, Sci. Rep. 5 (2015) 8403.
[44] Y.-F. Deng, S.-X. Zhao, Y.-H. Xu, K. Gao, C.-W. Nan, Chem. Mater. 27 (2015) 7734–7742.
[45] D. Mohanty, J. Li, D.P. Abraham, A. Huq, E.A. Payzant, D.L. Wood, C. Daniel, Chem. Mater. 26 (2014) 6272–6280.
[46] Y. Gao, J.R. Dahn, J. Electrochem. Soc. 6 (1996) 1783–1788.
[47] M.M. Thackeray, Prog. Solid State Chem. 25 (1997) 1–71.
[48] J.M. Paulsen, J.R. Dahn, Chem. Mater. 11 (1999) 3065–3079.
[49] B. Ammundsen, J.R. Re, M.S. Islam, J. Phys. Chem. B. 101 (1997) 8156–8163.
[50] S. Muhammad, H. Kim, Y. Kim, D. Kim, J.H. Song, J. Yoon, J.-H. Park, S.-J. Ahn, S.-H. Kang, M.M. Thackeray, W.-S. Yoon, Nano Energy 21 (2016) 172–184.
[51] Y.-P. Deng, F. Fu, Z.-G. Wu, Z.-W. Yin, T. Zhang, J.-T. Li, L. Huang, S.-G. Sun, J. Mater. Chem. A 4 (2016) 257–263.
[52] K. Luo, M.R. Roberts, R. Hao, N. Guerrini, D.M. Pickup, Y.-S. Liu, K. Edström, J. Guo, A.V. Chadwick, L.C. Duda, P.G. Bruce, Nat. Chem. 8 (2016) 684–691.
[53] H. Duncan, B. Hai, M. Leskes, C.P. Grey, G. Chen, Chem. Mater. 26 (2014) 5374–5382.
[54] S.-T. Myung, S. Komaba, N. Kumagai, H. Yashiro, H.-T. Chung, T.-H. Cho, Electrochim. Acta 47 (2002) 2543–2549.
[55] S. Ardizzone, C.L. Bianchi, D. Tirelli, Colloids Surf. A: Physicochem. Eng. Asp. 134 (1998) 305–312.
[56] B. Song, Z. Liu, M.O. Lai, L. Lu, Phys. Chem. Chem. Phys. 14 (2012) 12875–12883.
[57] D. Ye, K. Ozawa, B. Wang, D. Hulicova-Jurcakova, J. Zou, C. Sun, L. Wang, Nano Energy 6 (2014) 92–102.
[58] Y. Xiang, Z. Yin, Y. Zhang, X. Li, Electrochim. Acta 91 (2013) 214–218.
[59] P.K. Nayak, J. Grinblat, M. Levi, E. Levi, S. Kim, J.W. Choi, D. Aurbach, Adv. Energy Mater. 6 (2016) 1502398.
[60] Y. Wang, Z. Yang, Y. Qian, L. Gu, H. Zhou, Adv. Mater. 27 (2015) 3915–3920.
[61] J. Liu, M. Hou, J. Yi, S. Guo, C. Wang, Y. Xia, Energy Environ. Sci. 7 (2014) 705–714.
[62] J.R. Croy, M. Balasubramanian, K.G. Gallagher, A.K. Burrell, Acc. Chem. Res. 48 (2015) 2813–2821.

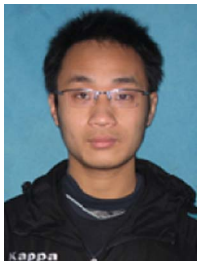

Yi Pei is a Ph.D candidate at the Department of Material Sciences and Engineering at Harbin Institute of Technology (HIT) under supervision of Prof. Liang Zhen. He has been a joint Ph.D student in the group of Prof. Guozhong Cao at the University of Washington at Seattle (UW) from 2014 to 2016. He received his master's degree in Material Science from Harbin Institute of Technology (HIT). His research interests focus on cathode materials for rechargeable alkali-ion batteries, especially for Li, Na and Mg-ion batteries.

Qing Chen is a Ph.D candidate at the Department of Material Sciences and Engineering at Harbin Institute of Technology (HIT) under supervision of Prof. Liang Zhen. She has been a joint Ph.D student in the group of Prof. Graeme Henkelman at University of Texas at Austin (UT) from 2014 to 2016. She received her master's degree in Condensed Matter Physics from Harbin Normal University. Her research interests focus on DFT calculations of cathode materials in lithium or sodium batteries and MD simulations of amorphous materials.

Yu-Chen Xiao is a Ph.D candidate at the Department of Material Sciences and Engineering at Harbin Institute of Technology (HIT) under supervision of Prof. Liang Zhen. He received his master's degree in Material Science in 2014 from Harbin Institute of Technology (HIT). His research interests focus on anode materials for lithium or sodium-ion batteries.

Prof. Li Liu is a full professor at School of Chemistry, Xiangtan University. She received her Ph.D. degree in 2009 from Nankai University. She was a visiting scholar in Prof. Guozhong Cao's group at University of Washington in Seattle (UW) from 2015 to 2016. Her research interests focus on electrode materials for rechargeable alkali-ion batteries, especially for Li and Na-ion batteries.

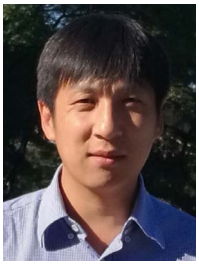

Prof. Cheng-Yan Xu is a full professor at School of Material Sciences and Engineering, Harbin Institute of Technology. He received his bachelor degree in 2000 and Ph.D. degree in 2008 from Harbin Institute of Technology. He was a visiting student with Prof. Lu-Chang Qin at UNC Chapel Hill from 2004 to 2005, and a visiting scholar in Prof. Zhong Lin Wang's group at Georgia Tech. His research interests focus on two-dimensional materials and their applications in energy, optoelectronics, and biology.

Prof. Liang Zhen is a Chang Jiang Scholars professor at School of Material Sciences and Engineering, Harbin Institute of Technology. He earned his bachelor degree from Hebei Institute of Technology in 1986, master and PhD degrees from Harbin Institute of Technology in 1991 and 1994, respectively. His research involves structure-property relationships of both bulk and low-dimensional materials, such as alloys, oxides, and chalcogenides.

Prof. Graeme Henkelman is a professor of Chemistry and the Director of the Center for Computational Molecular Sciences in the Institute for Computational Engineering and Sciences at the University of Texas at Austin. He graduated with a degree in Physics from Queen's University in Canada, and a Ph.D. in Chemistry from the University of Washington. The Henkelman research group focuses on computational method for modeling reaction dynamics in chemical and material systems with a focus on energy applications.

Prof. Guozhong Cao is Boeing-Steiner Professor of materials science and engineering, professor of chemical engineering, and adjunct professor of mechanical engineering at the University of Washington, and also a professor at Beijing Institute of Nanoenergy and Nanosystems, Chinese Academy of Sciences and Dalian University of Technology. His current research is focused on chemical processing of nanomaterials for energy related applications including solar cells, rechargeable batteries, supercapacitors, and hydrogen storage.